Journal of Catalysis **196,** 56–65 (2000)
doi:10.1006/jcat.2000.3033, available online at http://www.idealibrary.com on IDEAL®

Supported Gold Catalysts Prepared from a Gold Phosphine Precursor and As-Precipitated Metal-Hydroxide Precursors: Effect of Preparation Conditions on the Catalytic Performance

Alexander I. Kozlov,* Anguelina P. Kozlova,* Kiyotaka Asakura,*,[1] Yoshio Matsui,† Toshihiro Kogure,‡ Takafumi Shido,* and Yasuhiro Iwasawa*,[2]

*Department of Chemistry, Graduate School of Science, The University of Tokyo, Hongo, Bunkyo-ku, Tokyo 113-0033, Japan; †National Institute for Research in Inorganic Materials, 1-1 Namiki, Tsukuba, Ibaraki 305-0044, Japan; and ‡Institute of Mineralogy, Graduate School of Science, The University of Tokyo, Hongo, Bunkyo-ku, Tokyo 113-0033, Japan

Received March 6, 2000; revised June 26, 2000; accepted August 21, 2000

Supported gold catalysts highly active for low-temperature CO oxidation were prepared by using $AuPPh_3NO_3$ complex as a Au-metal precursor and wet as-precipitated iron hydroxide and titanium hydroxide as support precursors. Effects of catalyst preparation conditions on the performance for low-temperature CO oxidation were studied. Metal-hydroxide precipitation conditions and heating rates of temperature-programmed calcination altered significantly the performance of the supported gold catalysts. To elucidate key factors responsible for the effects the catalysts were characterized by EXAFS, TEM, XRD, and N_2 adsorption. Changes in the activities of both Au/Fe oxide and Au/Ti oxide catalysts originated mainly from changes of the Au particle size distribution. It was also found that states of the mesoporous support precursors upon attaching the Au precursor onto them and during the temperature-programmed calcination appeared to be of great importance in obtaining dispersed Au nanoparticles on oxide surfaces.

Key Words: **gold catalysts; preparation method; low-temperature CO oxidation; supported Au–phosphine complex; iron oxide; titanium oxide.**

1. INTRODUCTION

The longer challenge to catalyst preparation of oxide-supported metal catalysts is to address important issues in regulation of size and distribution of metal particles. Distinct materials and chemistry prepared stepwise in a controllable manner by using organic and inorganic metal complexes or clusters as precursors have provided an opportunity for development of efficient catalytic surfaces (1–7). However, the superiority of this kind of preparation method, where Au-complex precursors are attached on oxide surfaces, followed by further treatment to obtain active gold metal ensembles, cannot be applied to supported Au catalytic systems due to easy sintering of Au species to grow to large Au particles.

Novel high reactivity of matrix-trapped Au atoms for CO oxidation at 30–40 K has been discovered by Ozin and his coworkers (8). In the 1990s supported Au catalysts have been successfully applied to industrial reactions, while fundamental researches on catalytic properties of Au-based materials have been conducted extensively interlacing with industrial curiosity (9–22). Although there are several reports about the activity of oxidic gold species (21, 23–25), most researchers have ascribed the high performance of supported Au catalysts to small metallic Au nanoparticles (9–16, 18, 26–36). Extensive studies on a variety of supported gold catalysts have demonstrated a decisive role of preparation method in stabilization of finely dispersed Au.

In 1996 we reported a novel efficient method for preparation of active supported gold catalysts using wet as-precipitated metal hydroxides ($M(OH)_x^*$) and gold phosphine complexes as precursors for oxide supports and gold particles, respectively (37). A $Au/Fe(OH)_3^*$ catalyst is one of the most active Au catalysts reported until now, showing a high CO oxidation activity even at 203 K (10, 22, 37–39) (Table 1). A crucial role of the interaction of Au complexes and support precursors in obtaining active catalysts was evident for $Au/Fe(OH)_3^*$ and $Au/Ti(OH)_4^*$ catalysts (10, 38–40), which suggests a possibility of being able to control Au particle size through preparation conditions.

In the present study EXAFS, TEM, XRD, and N_2 adsorption measurements were employed to elucidate an effect of preparation conditions on the performances of $Au/Fe(OH)_3^*$ and $Au/Ti(OH)_4^*$ catalysts in low-temperature CO oxidation. The choices of precipitation reagent and calcination-heating rate altered significantly the catalytic performance of $Au/Fe(OH)_3^*$. The key issues, such as Au particle size distribution, mesoporous support precursor,

[1] Present address: Catalysis Research Center, Hokkaido University, Kita-ku, Sapporo 060-0811, Japan.

[2] To whom correspondence should be addressed. Fax: 81-3-5800-6892. E-mail: iwasawa@chem.s.u-tokyo.ac.jp.

0021-9517/00 $35.00

TABLE 1

CO Oxidation on Iron Oxide-Supported Au Catalysts

Catalyst	Preparation method[a]	Au particle size (nm)	T (K)	Rate (mol CO (mol-Au)$^{-1}$ s^{-1})	E_a (kcal mol^{-1})	TOF (207 K) $\times 10^3$ (s^{-1})[b]	Ref.
Au(3 wt%)/Fe(OH)$_3^*$-S-4	IAH	2.6	207	8.5×10^{-3}	6.8	17.9	This work
Au(3 wt%)/Fe(OH)$_3^*$-A-0.1	IAH	3.4	207	3.6×10^{-3}	—	10.2	This work
Au(3 wt%)/Fe(OH)$_3^*$-A-4	IAH	4.9	207	1.6×10^{-3}	—	6.4	This work
Au(3 wt%)/Fe(OH)$_3^*$	IAH	<4.0	268	9.6×10^{-3}	—	—	54
Au(3 wt%)/Fe$_2$O$_3^*$	IO	12	207	8.1×10^{-5}	5.0	0.79	22, 51
Au(5 wt%)/α-Fe$_2$O$_3$	IO	16.0	393	4.9×10^{-3}	—	—	20
Au(0.26 wt%)/α-Fe$_2$O$_3$	DP	Au$_2$O$_3$ + Au	363	4.7×10^{-1}	—	—	25
Au(0.26 wt%)/α-Fe$_2$O$_3$	DP	4.0	363	2.8×10^{-1}	—	—	25
Au(11.5 wt%)/Fe$_2$O$_3$	CP	3.6	203	2.6×10^{-3}	—	9.7–11.4[c]	49
Au(0.56 wt%)/Fe$_2$O$_3$	CP	AuOOH	207	6.3×10^{-4}	9.35	—	21, 52
Au(3.15 wt%)/Fe$_2$O$_3$	CP	6.5	207	2.4×10^{-4}	7.4	1.26	32
Au(5 wt%)/Fe$_2$O$_3$	CP	4.8	275	3.8×10^{-3}	—	—	36
Au(0.66 wt%)/Fe$_2$O$_3$	DP	—	207	4.6×10^{-5}	8.4	—	49
Au(3.15 wt%)/Fe$_2$O$_3$	CP	—	303	5.1×10^{-2}	—	—	53

[a] IAH, impregnation of the as-precipitated Fe hydroxides with the gold complex; IO, impregnation of Fe oxides; CP, coprecipitation; DP, deposition–precipitation.

[b] p(CO) = 1 kPa, p(O$_2$) = 20 kPa; TOFs were calculated using reported mean Au particle sizes and activation energies.

[c] TOF at 207 K was calculated assuming E_a in the range of 5.0–8.4 kcal mol^{-1}.

and Au-support interaction, to obtain active supported Au catalysts are discussed.

2. EXPERIMENTAL

2.1. Materials

Fe(NO$_3$)$_3 \cdot$ 9H$_2$O, Na$_2$CO$_3$, and 25%-NH$_4$OH (all, 99.9% purity) were purchased from Wako Chemicals. Authentic samples of iron oxide and titanium oxide polymorphs were supplied by Soekawa Chemicals and Wako Chemicals, respectively. Ti(i-OPr)$_4$ (99.99%) was received from Aldrich. AuPPh$_3$NO$_3$ was prepared according to the literature (41).

2.2. Catalyst Preparation

As-precipitated wet hydroxides were obtained by hydrolysis of Fe(NO$_3$)$_3 \cdot$ 9H$_2$O or Ti(i-OPr)$_4$ with an aqueous solution of Na$_2$CO$_3$ or NH$_4$OH. They are denoted in the text as M(OH)$_x^*$-S and M(OH)$_x^*$-A (M = Fe, Ti), respectively (10, 37–40). After supporting AuPPh$_3$NO$_3$ complex on the M(OH)$_x^*$-S and -A, the samples were temperature-programmed calcined at a given heating rate to 673 K and kept at 673 K for 4 h in a flow of dry air (30 ml min^{-1}) to give Au/M(OH)$_x^*$-S-R and Au/M(OH)$_x^*$-A-R catalysts (where R stands for a programmed heating rate of 20, 4, 0.5, or 0.1 K min^{-1}). Details of the preparation procedure have been reported (10, 22, 37–40). The Au loading was typically 3 wt%. Samples calcined at different temperature (T) are denoted as Au/M(OH)$_x^*$ (T). To examine the effect of PPh$_3$ ligand on support structure, a Fe(OH)$_3^*${P} sample was prepared by impregnation of Fe(OH)$_3^*$ with an acetone solution of PPh$_3$ instead of AuPPh$_3$NO$_3$.

2.3. Sample Characterization

TEM images of the Au/Fe(OH)$_3^*$ catalysts were observed using a Hitachi-1500 electron microscope operated at 800 kV, while images for Au/Ti(OH)$_4^*$ were taken using a Hitachi HF-2000 electron microscope at 200 kV. Samples were dispersed in ethanol or CCl$_4$ and a drop of the obtained suspension was fixed on a microgrid covered with amorphous carbon film.

Au L$_3$-edge EXAFS spectra were measured at room temperature in a transmission mode at BL-7C station of the Photon Factory of the Institute of Materials Structure Science, High Energy Accelerator Research Organization (KEK-PF) (Proposal 97-G040) and the data were analyzed by a "Rigaku EXAFS (REX)" program.

XRD patterns were recorded in the 2θ range from 20° to 80° at a scanning speed of 2°(2θ) min^{-1} on a Rigaku Miniflex X-ray diffractometer with nickel-filtered CuK_α radiation operated at 30 kV and 15 mA.

Nitrogen (N$_2$ 99.9999%) adsorption isotherms at 77 K were obtained on a BELSORP-28SA equipment. Before the measurements samples of about 0.3 g were pretreated in vacuum using a turbo molecular pump. The surface areas of the samples were estimated by the conventional BET method (42). Mesopore analysis was carried out using the Dollimore and Heal method (43).

2.4. Catalytic Performance

The catalytic performances at the steady-state were measured after 40 min on stream at each reaction temperature in the temperature ranges from 207 to 298 K for the Au/Fe(OH)$_3^*$ catalysts and from 273 to 503 K for the

$Au/Ti(OH)_4^*$ catalysts. In a typical experiment a gas mixture of 1.0% CO balanced with air was passed through 200 mg of a catalyst at a flow rate of 67 ml min^{-1}. The product analysis was performed by an on-line gas chromatograph.

3. RESULTS

3.1 Catalysts Derived from $AuPPh_3NO_3$ and As-Precipitated $Fe(OH)_3^*$

3.1.1. Catalytic performance. Figures 1 and 2 show the results of CO oxidation on $Au/Fe(OH)_3^*$ catalysts prepared under different precipitation and calcination conditions, respectively. All the $Au/Fe(OH)_3^*$ catalysts exhibited remarkably high activities for CO oxidation allowing 100% CO conversion at room temperature or below. Supporting $AuPPh_3NO_3$ on iron hydroxides precipitated by Na_2CO_3 at different pH resulted in $Au/Fe(OH)_3^*$ catalysts with similar catalytic performances to each other (Fig. 1). $Au/Fe(OH)_3^*$-A-4 catalyst obtained by using NH_4OH for support precipitation also showed a high level of CO conversion at room temperature, but the activity leveled off from the high performance with decreasing temperature. The $Au/Fe(OH)_3^*$-A-4 catalyst exhibited only 9% CO conversion at 207 K, while the conversion on the $Au/Fe(OH)_3^*$-S-4 catalyst was as high as 52% at the same temperature (Fig. 1). Heating rate during the temperature-programmed calcination changed the catalytic activity of $Au/Fe(OH)_3^*$ profoundly. Performances of the $Au/Fe(OH)_3^*$ catalysts were improved by applying slower heating rates as shown in Fig. 2.

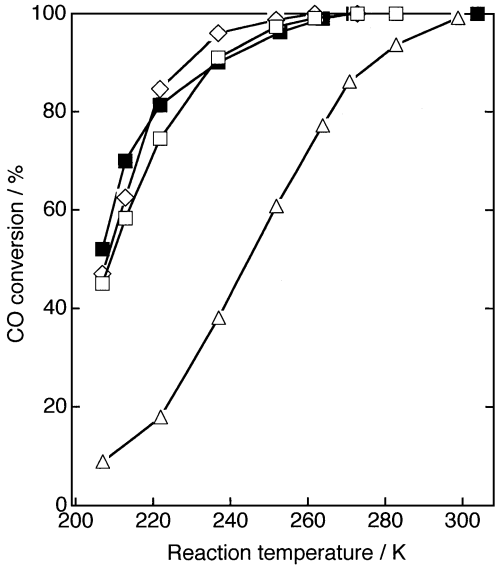

FIG. 1. CO oxidation on the $Au/Fe(OH)_3^*$ catalysts derived from as-precipitated $Fe(OH)_3^*$ obtained under different pH: (■) $Au/Fe(OH)_3^*$-S-4 at pH 9.1, (◇) $Au/Fe(OH)_3^*$-S-4 at pH 10.0, (□) $Au/Fe(OH)_3^*$-S-4 at pH 7.6, (△) $Au/Fe(OH)_3^*$-S-4 at pH 9.1.

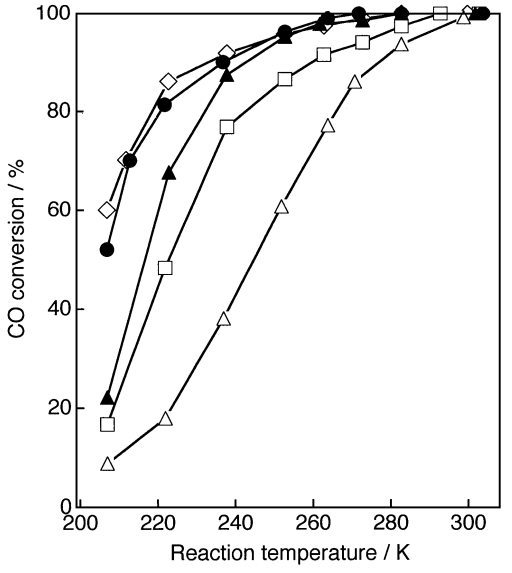

FIG. 2. CO oxidation on the $Au/Fe(OH)_3^*$ catalysts calcined at different heating rates. $Fe(OH)_3^*$ was obtained at pH 9.1: (◇) $Au/Fe(OH)_3^*$-S-0.5, (△) $Au/Fe(OH)_3^*$-A-4, (●) $Au/Fe(OH)_3^*$-S-4, (▲) $Au/Fe(OH)_3^*$-A-0.1, (□) $Au/Fe(OH)_3^*$-S-20.

Table 1 lists reaction rates, turnover frequencies (TOFs) and activation energies for the CO oxidation on iron oxide supported catalysts prepared by different methods. The TOFs were calculated on the basis of number of surface Au atoms which were estimated from mean Au particle sizes assuming a hemispherical shape of the particles. The $Au/Fe(OH)_3^*$-S-4 sample exhibited the highest catalytic performance at 207 K. The reaction rate of CO oxidation on the Au(3 wt%)/$Fe(OH)_3^*$-S-4 catalyst was 8.5×10^{-4} mol-CO (mol-Au)$^{-1}$ s^{-1} at 207 K, which was much higher than 2.4×10^{-4} mol-CO (mol-Au)$^{-1}$ s^{-1} at 207 K for Au (3.15 wt%)/Fe_2O_3 prepared by a traditional co-precipitation method (32) (Table 1).

3.1.2. State of support. XRD patterns for $Au/Fe(OH)_3^*$ and iron oxide supports calcined at 673 K are shown in Fig. 3. General features of XRD patterns for all the $Au/Fe(OH)_3^*$ catalysts were appearance of γ-Fe_2O_3 phase and poorer crystallinity as compared to $Fe_2O_3^*$-S-4 prepared by calcination of as-precipitated $Fe(OH)_3^*$-S. $Fe(OH)_3^*${P}-S-4, $Au/Fe(OH)_3^*$-S-4, and $Au/Fe(OH)_3^*$-A-4 exhibited essentially the same XRD patterns, indicating similar content of the γ-Fe_2O_3 phase. There is a clear correlation between the heating rate and the content of γ-phase. The slower the heating rate, the smaller the amount of γ-Fe_2O_3 phase became. Au(111) peak was hard to detect in all the catalysts.

Figures 4 and 5 show adsorption-desorption cycles of nitrogen at 77 K for the $Au/Fe(OH)_3^*$-S and $Au/Fe(OH)_3^*$-A catalysts calcined at different temperatures, respectively. Types of adsorption isotherms, specific BET surface areas and mean pore sizes for the examined $Au/Fe(OH)_3^*$ samples together with other characterization

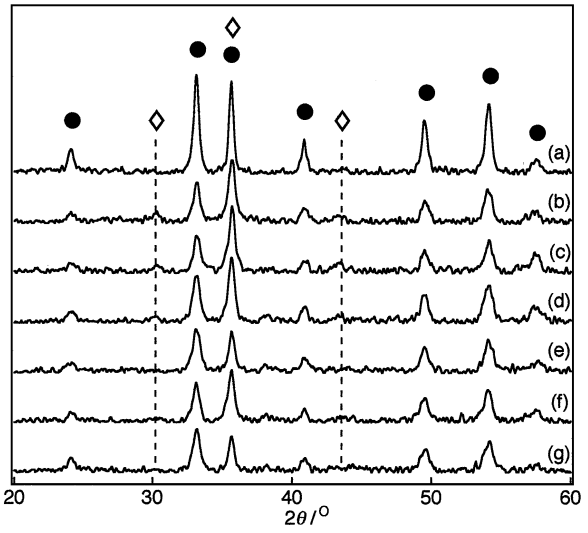

FIG. 3. XRD patterns of the Au/Fe(OH)$_3^*$ catalysts: (a) Fe$_2$O$_3^*$-S-4, (b) Fe(OH)$_3^*${P}-S-4, (c) Au/Fe(OH)$_3^*$-S-20, (d) Au/Fe(OH)$_3^*$-S-4, (e) Au/Fe(OH)$_3^*$-S-0.5, (f) Au/Fe(OH)$_3^*$-A-4, and (g) Au/Fe(OH)$_3^*$-A-0.1. ◇ and ● indicate γ-Fe$_2$O$_3$ and α-Fe$_2$O$_3$, respectively.

data are listed in Table 2. The nitrogen adsorption isotherms of Au/Fe(OH)$_3^*$-S (RT), Au/Fe(OH)$_3^*$-S-4 (423), and Au/Fe(OH)$_3^*$-S-4 (473) samples can be described as type II of IUPAC classification (Table 2 and Fig. 4) (44). The samples possessed mesopores of ca. 5 nm with the distribution of 2–15 nm in diameter and exhibited hysteresis loops of type H2 with closure point at P/P_0 as low as 0.45. In contrast to the Au/Fe(OH)$_3^*$-S samples, Au/Fe(OH)$_3^*$-A (RT), Au/Fe(OH)$_3^*$-A-4 (423), Au/Fe(OH)$_3^*$-A-4 (473), and Au/Fe(OH)$_3^*$-A-0.1 (473) samples possessed mainly micropores, showing adsorption isotherms which resemble type I of IUPAC classification with narrow H4 type hysteresis. Gradual dehydration of the iron oxide support up

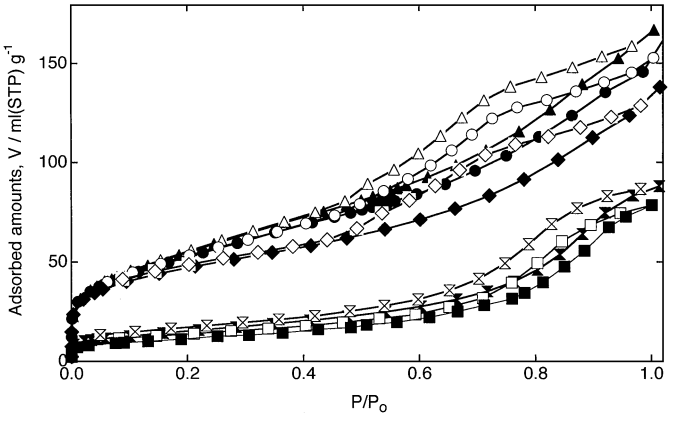

FIG. 4. N_2 adsorption isotherms and hysteresis loops at 77 K for the Au/Fe(OH)$_3^*$-S samples. Closed and open symbols correspond to adsorption and desorption steps, respectively: (◆) (◇) Au/Fe(OH)$_3^*$ (RT), (▲) (△) Au/Fe(OH)$_3^*$-S (423), (●) (○) Au/Fe(OH)$_3^*$-S (473), (⊠) (⧗) Au/Fe(OH)$_3^*$-S (573), (■) (□) Au/Fe(OH)$_3^*$-S (673).

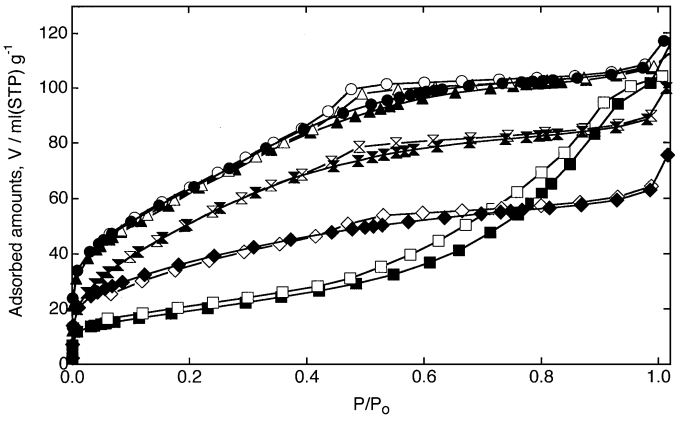

FIG. 5. N_2 adsorption isotherms and hysteresis loops for the Au/Fe(OH)$_3^*$-A samples. Closed and open symbols correspond to adsorption and desorption steps, respectively: (◆) (◇) Au/Fe(OH)$_3^*$-A (RT), (▲) (△) Au/Fe(OH)$_3^*$-A-4 (423), (●) (○) Au/Fe(OH)$_3^*$-A-4 (473), (⊠) (⧗) Au/Fe(OH)$_3^*$-A-0.1 (473), (■) (□) Au/Fe(OH)$_3^*$-A-4 (673).

to 473 K proceeded with retention of the pore structure of the corresponding as-precipitated materials. Crystallization of the support at temperatures >573 K was accompanied with remarkable decreasing the surface area and increasing the averaged pore size for both Au/Fe(OH)$_3^*$-S-4 and Au/Fe(OH)$_3^*$-A-4 catalysts. The Au/Fe(OH)$_3^*$-S-4 (673) catalyst exhibited type IV isotherm with H3 type of hysteresis, while the isotherm for Au/Fe(OH)$_3^*$-A-4 (673) catalyst was of type IV with the hysteresis loop of H1 shape. Raising the calcination temperature from 573 to 773 K resulted in decrease of the surface area for Au/Fe(OH)$_3^*$-S-4 and increase of the average pore size due to disappearance of a fraction of mesopores <6 nm in diameter.

3.1.3. State of gold. Table 3 shows the results of curve-fitting analysis of the Au L_3-edge EXAFS data for the Au/Fe(OH)$_3^*$-S (673) and Au/Fe(OH)$_3^*$-A (673) samples treated at heating rates of 0.1–20 K min^{-1} from room temperature to 673 K. The Au–Au bond distances for all the Au/Fe(OH)$_3^*$ catalysts except the Au/Fe(OH)$_3^*$-A-0.1 catalyst were similar to 0.287 nm for Au foil. Coordination numbers were in the range of 7.7–10.0 and tended to decrease when slow heating rates were applied. The values are significantly smaller than the value ($N = 12$) for Au foil. The results demonstrate that Au atoms aggregate with each other to form metallic particles. The larger coordination number (10.0 ± 1.4) for Au/Fe(OH)$_3^*$-A-4 compared to that (7.9 ± 1.2) for Au/Fe(OH)$_3^*$-S-4 indicates the formation of bigger Au metallic particles in the former catalyst.

Size distributions of Au metallic particles in typical Au/Fe(OH)$_3^*$ catalysts were estimated by TEM. Figure 6 shows the histograms of Au particle distributions in the Au/Fe(OH)$_3^*$-S-4, Au/Fe(OH)$_3^*$-A-4, and Au/Fe(OH)$_3^*$-A-0.1 catalysts. All the catalysts exhibited the high population of Au particles less than 5 nm. The Au/Fe(OH)$_3^*$-S-4 catalyst

TABLE 2

Characterization of Typical Iron Oxide-Supported Au Catalysts

Catalyst	Isoterm type and hysteresis shape	S_{BET} ($m^2\ g^{-1}$)	Mean pore diameter (nm)	Fe oxide[a]	State of Au[b]
Au/Fe(OH)$_3^*$-S (RT)	II/H2	164	5.5	Amorphous	$[AuPPh_3]^+$
Au/Fe(OH)$_3^*$-S-4 (473 K)	II/H2	186	4.8	Amorphous	$Au^0 + [AuPPh_3]^+$
Au/Fe(OH)$_3^*$-S-4 (573 K)	IV/H1	54	9.3	α-Fe_2O_3 + γ-Fe_2O_3	Au^0
Au/Fe(OH)$_3^*$-S-4 (673 K)	IV/H1	50	9.7	α-Fe_2O_3 + γ-Fe_2O_3	Au^0, 2.6 nm
Au/Fe(OH)$_3^*$-S-20 (673 K)	IV/H1	54	9.7	α-Fe_2O_3 + γ-Fe_2O_3	Au^0
Au/Fe(OH)$_3^*$-S-4 (773 K)	IV/H1 or H3	39	10.4	α-Fe_2O_3	Au^0
Au/Fe(OH)$_3^*$-A-4 (RT)	I/H4	130	3.1	Amorphous	$[AuPPh_3]^+$
Au/Fe(OH)$_3^*$-A-4 (473 K)	I/H4	226	2.9	Amorphous	$Au^0 + [AuPPh_3]^+$
Au/Fe(OH)$_3^*$-A-0.1 (473 K)	I/H4	193	2.8	Amorphous	—
Au/Fe(OH)$_3^*$-A-4 (673 K)	IV/H3	68	8.3	α-Fe_2O_3 + γ-Fe_2O_3	Au^0, 4.9 nm

[a] From XRD.
[b] From XPS, EXAFS, and TEM (this work and Ref. 39).

showed a sharpest size distribution where about 80% of Au particles ranged from 2 to 3 nm in diameter. For the Au/Fe(OH)$_3^*$-A-4 catalyst a broad multimodal Au particle size distribution was observed (Fig. 6a). The population of Au particles <3 nm was as small as 32%. The mean Au particle size in the Au/Fe(OH)$_3^*$-A-4 catalyst was 4.9 nm that was about two times larger than 2.6 nm in the Au/Fe(OH)$_3^*$-S catalyst. Au particle growth in the Au/Fe(OH)$_3^*$ seems to be simply controlled by varying heating rates. Although the Au/Fe(OH)$_3^*$-A-0.1 catalyst exhibited Au particles in the range 1–17 nm, a relatively sharp peak in the Au particle size distribution was located at about 2 nm and the fraction of particles <3 nm was as large as 67%. In contrast, the Au/Fe(OH)$_3^*$-A-4 catalyst possessed no Au particles smaller than 2 nm.

3.2. Catalysts Derived from $AuPPh_3NO_3$ and $Ti(OH)_4^*$

The catalytic activities of Au/Ti(OH)$_4^*$ catalysts in the steady-state CO oxidation are plotted as a function of reaction temperature in Fig. 7. The catalytic activities of the Au/Ti(OH)$_4^*$ samples were lower as compared with those the Au/Fe(OH)$_3^*$ samples. In contrast to the case of the Au/Fe(OH)$_3^*$ catalysts, the kind of precipitation reagent gave negligible effect on the performance of the Au/Ti(OH)$_4^*$ catalysts. CO conversions at 298 K on the Au/Ti(OH)$_4^*$-S-4 and Au/Ti(OH)$_4^*$-A-4 catalysts were 23 and 25%, respectively. Applying slowest heating rates for calcination resulted in the highest performance of the Au/Ti(OH)$_4^*$-S catalyst. The Au/Ti(OH)$_4^*$-S catalysts heated at 20, 4, and 0.1 K min^{-1} exhibited 12, 25, and 42% CO conversions at 298 K, respectively.

The Au/Ti(OH)$_4^*$-S (673) catalysts exhibited a mesoporous structure with surface area of about 80 $m^2\ g^{-1}$. XRD patterns of Au/Ti(OH)$_4^*$-S-0.1, Au/Ti(OH)$_4^*$-S-4, and Au/Ti(OH)$_4^*$-S-20 are shown in Fig. 8. The Au/Ti(OH)$_4^*$-S-0.1 and Au/Ti(OH)$_4^*$-S-4 catalysts exhibited only XRD peaks characteristic of Au metal, revealing amorphous structure of the titania support. In addition to gold diffraction peaks, the Au/Ti(OH)$_4^*$-S-20 catalyst showed the XRD peaks due to anatase (25.2°, 48.0°, and 62.7°) and rutile (27.5°, 36.2°, 41.3°, 54.4°, and 69.2°). Lines at 29.8°, 33.0°, 58.1°, and 67.0° may tentatively be prescribed to reduced titania phases (45). In the case of iron oxide-supported Au catalysts signal-to-noise ratio was not sufficient due to fluorescence background of the iron oxide support. On the other hand, the absence of intensive background in the Au/Ti(OH)$_4^*$ catalysts due to amorphous/poorly crystallized state of the support gave relatively high signal-to-noise ratio, which allowed to observe clearly all the Au reflections.

TABLE 3

Curve-Fitting Results for the Au L_3-Edge EXAFS Data of Au/Fe(OH)$_3^*$ Samples Calcined at 673 K

Catalyst	Bond	N	r (nm)	$\Delta\sigma^2$ (nm^2)	ΔE (eV)
Au/Fe(OH)$_3^*$-S-0.5	Au–Au	7.7 ± 1.3	0.285 ± 0.002	$31 \pm 10 \times 10^{-6}$	2 ± 8
Au/Fe(OH)$_3^*$-S-4	Au–Au	7.9 ± 1.2	0.287 ± 0.002	$18 \pm 10 \times 10^{-6}$	2 ± 3
Au/Fe(OH)$_3^*$-S-20	Au–Au	10.0 ± 1.3	0.287 ± 0.002	$11 \pm 10 \times 10^{-6}$	1 ± 5
Au/Fe(OH)$_3^*$-A-0.1	Au–Au	8.2 ± 1.3	0.283 ± 0.002	$20 \pm 10 \times 10^{-6}$	-4 ± 5
Au/Fe(OH)$_3^*$-A-4	Au–Au	10.0 ± 1.4	0.285 ± 0.003	$14 \pm 10 \times 10^{-6}$	0 ± 6

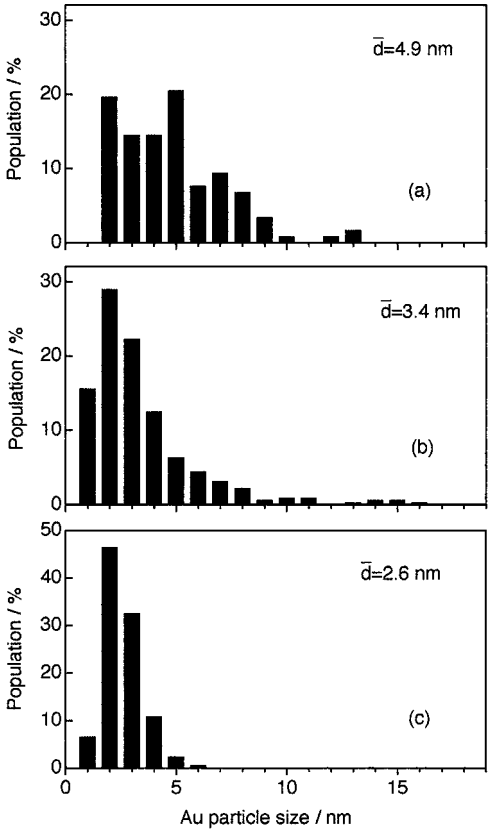

FIG. 6. Size distributions of Au metallic particles in the (a) Au/$Fe(OH)_3^*$-A-4, (b) Au/$Fe(OH)_3^*$-A-0.1, and (c) Au/$Fe(OH)_3^*$-S-4 catalysts as estimated by TEM.

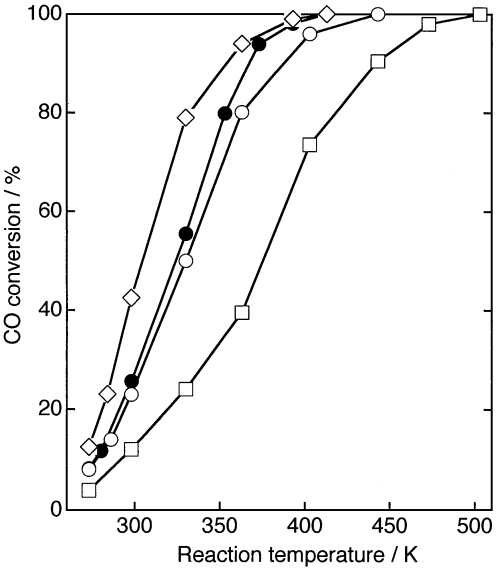

FIG. 7. CO oxidation on the differently prepared Au/$Ti(OH)_4^*$ catalysts: effects of precipitation reagent and calcination-heating rate: (○) Au/$Ti(OH)_4^*$-S-4, (□) Au/$Ti(OH)_4^*$-S-20, (●) Au/$Ti(OH)_4^*$-A-4, (◇) Au/$Ti(OH)_4^*$-S-0.1.

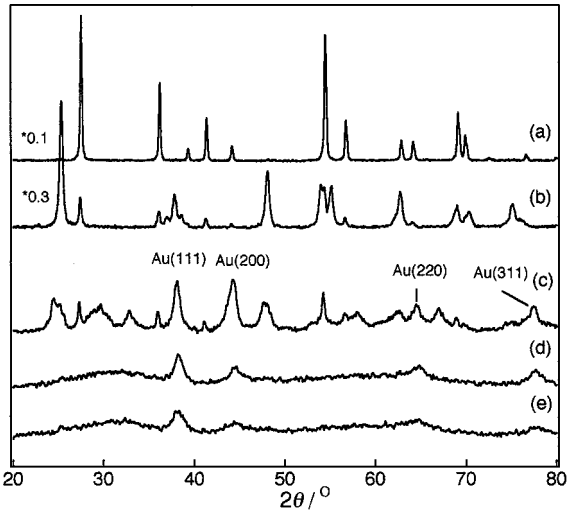

FIG. 8. XRD patterns of (a) TiO_2-rutile, (b) TiO_2-anatase, (c) Au/$Ti(OH)_4^*$-S-20, (d) Au/$Ti(OH)_4^*$-S-4, and (e) Au/$Ti(OH)_4^*$-S-0.1 catalysts.

Au particle size distributions in the Au/$Ti(OH)_4^*$-S (673) catalysts calcined at different heating rates are shown in Fig. 9. The histogram for the Au/$Ti(OH)_4^*$-S-0.1 catalyst revealed a relatively narrow distribution feature as compared with that for the Au/$Ti(OH)_4^*$-S-20 catalyst which consisted

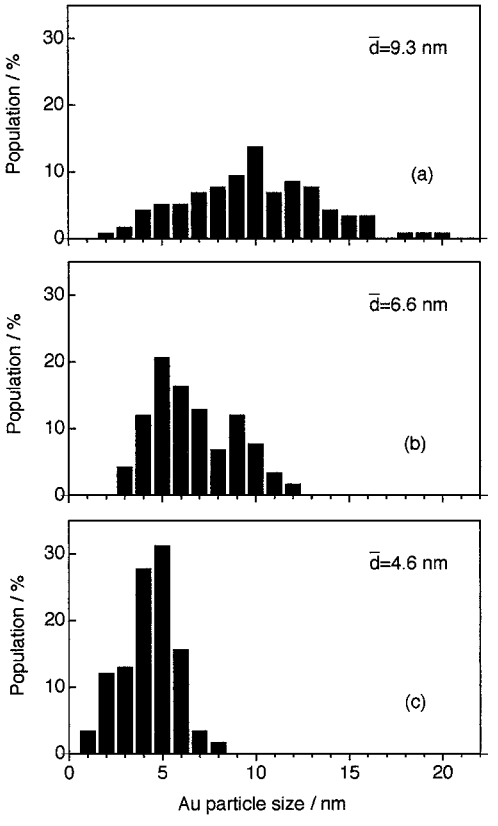

FIG. 9. Size distributions of Au metallic particles in the (a) Au/$Ti(OH)_4^*$-S-20, (b) Au/$Ti(OH)_4^*$-S-4, and (c) Au/$Ti(OH)_4^*$-S-0.1 catalysts as estimated by TEM.

of Au particles of 2–20 nm in diameter. A bimodal distribution with maxima at 5 and 9 nm was observed with the Au/Ti(OH)$_4^*$-S-4 catalyst. The averaged Au-particle sizes for Au/Ti(OH)$_4^*$-S-0.1, Au/Ti(OH)$_4^*$-S-4, and Au/Ti(OH)$_4^*$-S-20 were estimated to be 4.6, 6.6, and 9.3 nm, respectively.

4. DISCUSSION

Dispersion of Au metal on oxide supports have been considered to be one of the main factors affecting the catalytic performances in various reactions (9–11). Since Au has a low melting point, it undergoes readily to sintering, and hence strong interaction with the support is demanded for stabilization of fine Au particles. Choice of an appropriate preparation method may be more important to obtain fine Au particles on oxide supports than in the cases of other noble metal catalysts. The newly developed method to prepare highly active Au catalysts for low-temperature CO oxidation by using Au phosphine complexes and as-precipitated wet metal hydroxides is efficient particularly to produce extremely active Au catalysts supported on Fe, Mn, Co, Ni, and Zn oxides (10, 22, 37–40).

Interactions between a gold precursor and a support precursor have been proved to be crucial for obtaining active supported gold catalysts (10, 22, 38–40). The activity of the Au/Fe(OH)$_3^*$ catalysts greatly depended on the nature of a Au complex as well as the state of a support used for preparation. AuPPh$_3$NO$_3$ complex gave an extremely active catalyst when it was supported on as-precipitated iron hydroxide where efficient interactions of [AuPPh$_3$]$^+$ with surface O$^-$ and OH$^-$ groups (Scheme 1) were observed (10, 38, 39). The Au precursor–support precursor interaction would be affected by structural factors characteristic of metal hydroxide precipitates, such as surface area, pore size, and structural water, which may be determined in the precipitation stage. Unlike the coprecipitation method where both support state and nature of deposited Au species may be greatly altered by the precipitation conditions, our approach can exclude unknown effects of the precipitation conditions on the state of the Au precursor.

Figure 1 shows that the pH for precipitation of Fe(OH)$_3^*$ has a negligible effect on the activity of the Au/Fe(OH)$_3^*$-S-4 catalysts, which suggests the similarity of the states of supports. On the other hand, significant decrease in the catalytic activity was observed when NH$_4$OH was used instead of Na$_2$CO$_3$ as a precipitation reagent. The origin of the effect was elucidated by EXAFS, TEM, XRD, and N$_2$ adsorption measurements. The TEM analysis demonstrated that use of ammonia resulted in relatively larger Au particles in the Au/Fe(OH)$_3^*$-A-4 catalyst (4.9 nm mean size of Au particles) as compared with the Au/Fe(OH)$_3^*$-S-4 catalyst (2.6 nm mean size of Au particles). This trend in particle size was also indicated by the EXAFS curve fitting results which showed an increase in the coordination number (10.0) for

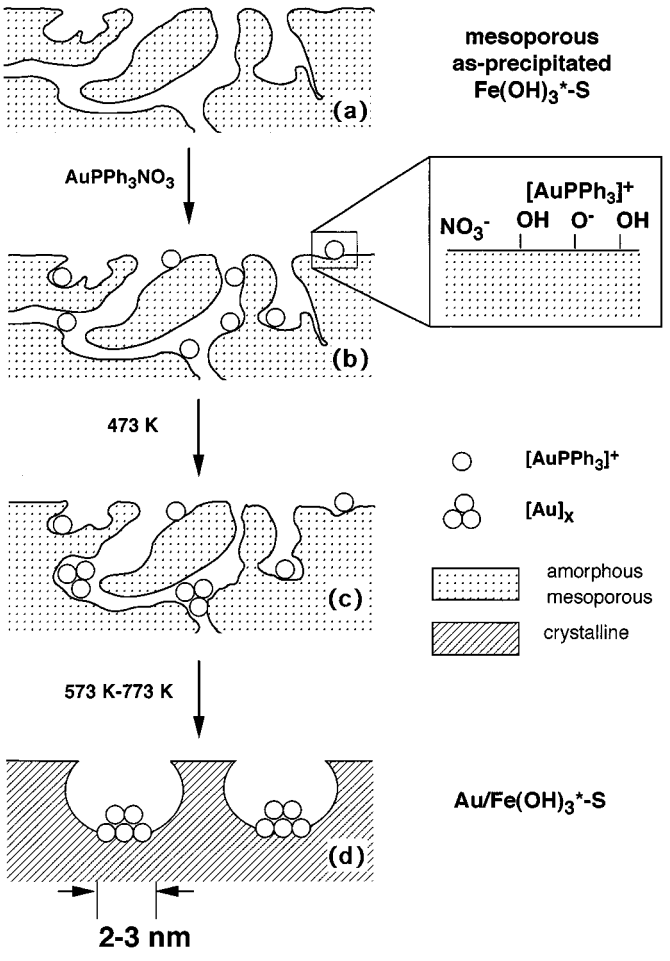

SCHEME 1. Transformation of support and gold precursors during temperature-programmed calcination.

Au–Au bond in the Au/Fe(OH)$_3^*$-A-4 catalyst as compared with that (7.9) for the Au/Fe(OH)$_3^*$-S-4 catalyst. The coordination numbers determined by EXAFS are smaller than those expected from the TEM mean particle sizes. This may be due to the disorder effect which gives asymmetrical distribution function and hence apparent reduction of the coordination number. This effect is larger with smaller particles. Thus the reduction of the coordination number for Au–Au bond indicates smaller particle sizes, which give the results compatible with the TEM results. Both catalysts exhibited similar XRD patterns characteristic of a mixture of poorly crystalline α-Fe$_2$O$_3$ and γ-Fe$_2$O$_3$ (Fig. 3). Moreover, the Au/Fe(OH)$_3^*$-A-4 (673) catalyst showed a higher surface area and a smaller mean pore diameter than those for the Au/Fe(OH)$_3^*$-S-4 catalyst. Thus, the higher surface area and smaller pore diameter in the final state of the support cannot be key issues to form smaller gold particles. Then we thought that a key issue might arise from the morphology/structure of Na$_2$CO$_3$-as-precipitated and NH$_4$OH-as-precipitated hydroxides. In fact, different states of the supports in the catalysts dried at RT are obvious from the

N_2 adsorption isotherms for Au/Fe(OH)$^*_3$-A and Au/Fe(OH)$^*_3$-S (Figs. 4 and 5), which are similar to those reported for poorly ordered and well-ordered ferrihydrites, respectively (46). Au/Fe(OH)$^*_3$-A (RT) was micro-mesoporous (3.1 nm in mean diameter) while Au/Fe(OH)$^*_3$-S (RT) exhibited a much larger mesoporous structure (5.5 nm) that may favor to homogeneous spreading of the Au precursor as illustrated in Scheme 1. Moreover, the surface area of Au/Fe(OH)$^*_3$-S-4 (164 $m^2\,g^{-1}$) was higher than that of Au/Fe(OH)$^*_3$-A-4 (130 $m^2\,g^{-1}$). The as-precipitated materials as well as the catalysts calcined at temperature below 573 K might have different content of structural water and accessible surface defects which are important in stabilization of the Au precursors and small Au particles (10, 38).

Our previous studies on the states of support and gold during calcination step showed that decomposition of the Au precursor and crystallization of the iron oxide support occurred in almost the same temperature range (10, 39). A similar conclusion can be drawn from the N_2 adsorption results (Figs. 4 and 5). Indeed, the N_2 adsorption isotherms of the catalysts calcined at 423 and 473 K revealed retention of the original structure of the supports, while calcination at temperatures higher than 573 K resulted in the formation of crystalline iron oxides with about four times lower surface area and bigger pore sizes (Table 2) as illustrated in Scheme 1. Importance of the calcination conditions for regulating the Au particle size in both Au/Fe(OH)$^*_3$ and Au/Ti(OH)$^*_4$ catalysts is evident from the TEM results (Figs. 6 and 9), which revealed that slow heating in the calcination process resulted in reduction of the gold particle size. The CO conversion was much larger when heating rate of 0.1 K min^{-1} instead of 4 K min^{-1} was used to calcine Au/Fe(OH)$^*_3$-A as shown in Fig. 2. The similar promoting effect of slow calcination was observed with Au/Fe(OH)$^*_3$-S and Au/Ti(OH)$^*_4$-S (Figs. 2 and 7).

The low-temperature CO oxidation on the Au/M(OH)$^*_x$ catalysts proceeds through activation of oxygen on oxide support and activation of CO on small Au particles (47, 48). Both gold particle size and support morphology/structure must be considered to clarify the origin of the observed change in the catalytic activity. Surface area and pore structure of the supports in the Au/Fe(OH)$^*_3$ (673) catalysts are not important issues to regulate the Au particles as discussed above. Moreover, careful consideration of the XRD patterns for the Au/Fe(OH)$^*_3$-S and Au/Fe(OH)$^*_3$-A catalysts calcined at 673 K (Fig. 3) reveals that changes in the catalytic performance is not due to the presence of γ-Fe_2O_3 phase. The CO oxidation rates were larger with the catalysts calcined at slower heating rates, while the amount of α-Fe_2O_3 phase was smaller. We have previously reported that the Au/Fe(OH)$^*_3$-S-4 catalysts calcined at 573, 673, and 773 K exhibit similar catalytic activities in spite of great difference in surface area, crystallinity of oxide-support, and content of γ-Fe_2O_3 (39) when the same precipitation reagent and heating rate are applied for the catalyst preparation. We suggest that the kind of precipitation reagent and the heating rate for calcination affect the catalytic performance due to preferable formation and stabilization of small Au metallic particles. Indeed the EXAFS and TEM studies strongly support the suggestion (Table 3 and Figs. 6 and 9). There is no evidence on the existence of oxidic (cationic) Au species in our active Au/M(OH)$_x$ catalysts because no Au–O bonding in all the samples was detected by the careful curve fitting analysis of the EXAFS data (Table 3). This agrees with the recent FT-IR study of CO adsorption and CO + O_2 reaction on the Au/Fe(OH)$^*_3$-S catalyst, where no characteristic bands of CO adsorbed on oxidic forms of gold have been detected (47). The particle size distributions for the Au/Fe(OH)$^*_3$ and Au/Ti(OH)$^*_4$ catalysts (Figs. 6 and 9) provide a basis for more precise comparison of the catalysts with different activities. The most active Au/Fe(OH)$^*_3$-S-4 and Au/Fe(OH)$^*_3$-A-0.1 catalysts possessed a high population of Au particles less than 3–4 nm, while the Au particle size distribution in the Au/Fe(OH)$^*_3$-A-4 catalyst with low activity (Fig. 6a) was broad (2–13 nm) with average particle size of 4.9 nm. Comparison of TOFs for the supported Au catalysts in Table 1 and Fig. 10 indicates that variation in the activity of both Au/Fe(OH)$^*_3$ and Au/Ti(OH)$^*_4$ catalysts cannot be explained by changes of surface area of Au particles. CO oxidation on Au-support interfacial sites suggested by Haruta *et al.* (49) seems to be a reasonable interpretation for the present catalytic results. It is to be noted that the data reported for coprecipitated catalysts (32, 49) and our data for the Au/Fe(OH)$^*_3$ catalysts are on the same line for the TOF vs diameter plots as shown Fig. 10.

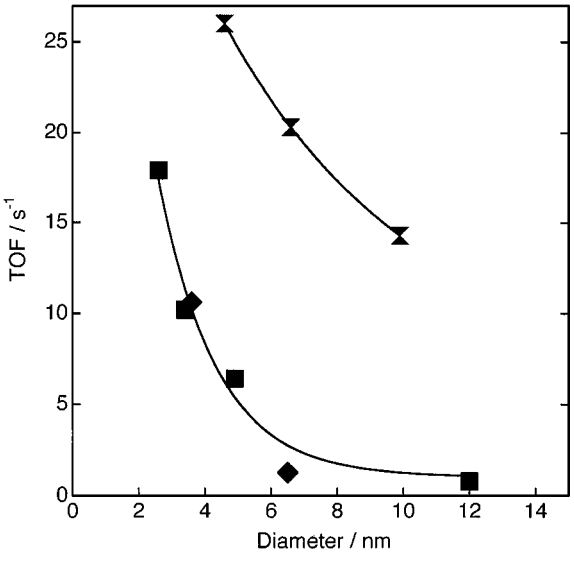

FIG. 10. Plots of TOF (s^{-1}) at 207 K (Au/Fe(OH)$^*_3$, Au/Fe_2O_3) or 298 K (Au/Ti(OH)$^*_4$) vs mean Au particle diameter by TEM for the supported Au catalysts; (■) Au/Fe(OH)$^*_3$, (◆) Au/Fe_2O_3, coprecipitated (32, 49), (⧗) Au/Ti(OH)$^*_4$.

In conclusion, the present approach to preparation of active supported gold catalysts provides a possibility to improve interactions between gold species and a support at all the stages of catalyst preparation. Scheme 1 illustrates the influence of iron hydroxide/oxide morphology/structure on the transformation of the $AuPPh_3NO_3$ complex to small Au particles in the preparation process of highly active $Au/Fe(OH)_3^*$-S catalysts. At the first step the wet as-precipitated support supplies numerous OH groups which stabilize the Au complex at RT and at early stages of the calcination. Lack of such stabilization in the case of the gold precursor supported on crystalline iron oxides results in large gold particles (22, 38, 39). A mesoporous structure of $Fe(OH)_3^*$ precipitated with Na_2CO_3 favored to a homogeneous distribution of the Au precursor on the high surface-area support (Scheme 1(b)). The structure of the $Fe(OH)_3^*$ support remains without significant change at least up to 473 K, at which temperature significant dehydration of the support occurs, resulting in loss of the stabilizing effect of OH groups and partial decomposition of the $AuPPh_3NO_3$ complex also occurs (39) as illustrated in Scheme 1(c). By increasing the calcination temperature to 473–573 K, crystallization and further dehydration of the support proceed to give iron oxide with many defects that may be responsible for inhibition of Au particle growth. Increasing amount of the defects can be caused by magnetite → magnemite → hematite transformations (50). The magnetite may be produced by reduction of the iron hydroxide/oxide support with the coexisting PPh_3 ligands. After calcination at 573–773 K (Scheme 1(d)) crystallization of the oxide support and complete decomposition of the $[AuPPh_3]^+$ species occur and small gold particles of 2–4 nm in diameter are produced on highly defective iron oxide surfaces. The initial state of the iron oxide precursor and its interaction with the Au precursor during the calcination are crucial in formation of small gold particles. The suggested Scheme 1 can be generally valid for other $Au/M(OH)_x^*$ catalysts derived from as-precipitated wet metal hydroxides and Au phosphine complexes.

ACKNOWLEDGMENTS

This work has been supported by Core Research for Evolutional Science and Technology (CREST) of Japan Science and Technology Corporation (JST).

REFERENCES

1. Iwasawa, Y., *Stud. Surf. Sci. Catal.* **101**, 21 (1996).
2. Iwasawa, Y., *Adv. Catal.* **35**, 187 (1987).
3. Iwasawa, Y., *in* "Tailored Metal Catalysts" (Y. Iwasawa, Ed.), p. 1. Riedel, Dordrecht, 1986.
4. Iwasawa, Y., *Catal. Today* **18**, 21 (1993).
5. Yamaguchi, A., Asakura, K., and Iwasawa, Y., *J. Mol. Catal. A* **146**, 65 (1999).
6. Gates, B. C., Guczi, L., and Knözinger, H. (Eds.), *in* "Metal Clusters in Catalysis." Elsevier, Amsterdam, 1986.
7. Thomas, J. M., *J. Mol. Catal. A* **115**, 371 (1997).
8. Huber, H., McIntosh, D., and Ozin, G. A., *Inorg. Chem.* **16**, 975 (1977).
9. Haruta, M., *Catal. Surv. J.* **1**, 61 (1997).
10. Kozlov, A. I., Kozlova, A. P., Liu, H., and Iwasawa, Y., *Appl. Catal. A* **182**, 9 (1999).
11. Bond, G. C., and Thompson, D. T., *Catal. Rev. Sci. Eng.* **41**, 319 (1999).
12. Hayashi, T., Tanaka, K., and Haruta, M., *J. Catal.* **178**, 566 (1998).
13. Nijhuis, T. A., Huizinga, B. J., Makkee, M., and Moulijn, J. A., *Ind. Eng. Chem. Res.* **38**, 884 (1999).
14. Prati, L., and Rossi, M., *J. Catal.* **176**, 552 (1998).
15. Sakurai, H., and Haruta, M., *Catal. Today* **29**, 361 (1996).
16. Andreeva, D., Idakiev, V., Tabakova, T., and Andreev, A., *J. Catal.* **158**, 354 (1996).
17. Nkosi, B., Adams, M. D., Coville, N. J., and Hutchings, G. J., *J. Catal.* **128**, 366 (1991).
18. Water, R. D., Weimer, J. J., and Smith, J. E., *Catal. Lett.* **30**, 181 (1995).
19. Ueda, A., and Haruta, M., *Appl. Catal. B* **18**, 453 (1998).
20. Haruta, M., Yamada, N., Kobayashi, T., and Iijima, S., *J. Catal.* **115**, 301 (1989).
21. Visco, A. M., Donato, A., Milone, C., and Galvagno, S., *React. Kinet. Catal. Lett.* **61**, 219 (1997).
22. Yuan, Y., Kozlova, A. P., Asakura, K., Wan, H., Tsai, K., and Iwasawa, Y., *J. Catal.* **170**, 191 (1997).
23. Finch, R. M., Hodge, N. A., Hutchings, G. J., Meagher, A., Pankhurst, Q. A., Siddiqui, M. R. H., Wagner, F. E., and Whyman, R., *Phys. Chem. Chem. Phys.* **1**, 485 (1999).
24. Visco, A. M., Neri, F., Neri, G., Donato, A., Milone, C., and Galvagno, S., *Phys. Chem. Chem. Phys.* **1**, 2869 (1999).
25. Park, E. D., and Lee, J. S., *J. Catal.* **186**, 1 (1999).
26. Bollinger, M. A., and Vannice, M. A., *Appl. Catal. B* **8**, 417 (1996).
27. Valden, M., Lai, X., and Goodman, D. W., *Science* **281**, 1647 (1998).
28. Shibata, M., Kawata, N., Masumota, T., and Kimura, H., *Chem. Lett.* 1605 (1985).
29. Baiker, A., Maciejewski, M., Tagliaferri, S., and Hug, P., *J. Catal.* **151**, 407 (1995).
30. Sayo, K., Deki, S., and Hayashi, S., *J. Mater. Chem.* **9**, 937 (1999).
31. Liu, W., and Flytzani-Stephanopoulos, M., *J. Catal.* **153**, 317 (1995).
32. Kahlich, M. J., Gateiger, H. A., and Behm, R. J., *J. Catal.* **182**, 430 (1999).
33. Blick, K., Mitrelias, T. D., Hargreaves, J. S. J., Hutchings, G. J., Joyner, R. W., Kiely, C. J., and Wagner, F. E., *Catal. Lett.* **50**, 211 (1998).
34. Grunwaldt, J. D., Kiener, C., Wogerbauer, C., and Baiker, A., *J. Catal.* **181**, 223 (1999).
35. Boccuzzi, F., Cerrato, G., Pinna, F., and Strukul, G., *J. Phys. Chem.* **B102**, 5733 (1998).
36. Tripathi, A. K., Kamble, V. S., and Gupta, N. M., *J. Catal.* **187**, 332 (1999).
37. Yuan, Y., Asakura, K., Wan, H., Tsai, K., and Iwasawa, Y., *Chem. Lett.* 755 (1996).
38. Kozlova, A. P., Sugiyama, S., Kozlov, A. I., Asakura, K., and Iwasawa, Y., *J. Catal.* **176**, 426 (1998).
39. Kozlova, A. P., Asakura, K., Kozlov, A. I., Sugiyama, S., Matsui, Y., and Iwasawa, Y., *J. Catal.* **181**, 37 (1999).
40. Yuan, Y., Asakura, K., Kozlova, A. P., Wan, H., Tsai, K., and Iwasawa, Y., *Catal. Today* **44**, 333 (1998).

41. Mueting, A. M., Alexander, B. D., Boyle, P. D., Casalnuovo, A. L., Ito, L. N., Johnson, B. J., and Pignolet, L. H., *in* "Inorganic Syntheses" (R. N. Grimes, Ed.), Vol. 29, p. 280. Wiley, New York, 1992.
42. Brunauer, S., Emmett, P. H., and Teller, E. J., *J. Am. Chem. Soc.* **60**, 309 (1938).
43. Dollimore, D., and Heal, G. R., *J. Colloid Interface Sci.* **33**, 508 (1970).
44. IUPAC Recommendations. Reporting Physisorption Data for Gas/Solid Systems. *Pure Appl. Chem.* **54**, 2201 (1982).
45. Anderson, S., Colen, B., Kuylenstierna, U., and Magneli, A., *Acta Chem. Scand.* **11**, 1641 (1957).
46. Cornell, R. M., and Schwertmann, U., "The Iron Oxides: Structure, Properties, Reactions, Occurrence and Uses," p. 362. VCH, Weinheim, 1996.
47. Liu, H. C., Kozlov, A. I., Kozlova, A. P., Shido, T., and Iwasawa, Y., *Phys. Chem. Chem. Phys.* **1**, 2851 (1999).
48. Liu, H., Kozlov, A. I., Kozlova, A. P., Shido, T., Asakura, K., and Iwasawa, Y., *J. Catal.* **185**, 264 (1999).
49. Haruta, M., Tsubota, S., Kobayashi, T., Kageyama, H., Genet, M. J., and Delmon, B., *J. Catal.* **144**, 175 (1993).
50. Feitknecht, W., *Mem. Sci. Rev. Metall.* **42**, 121 (1965).
51. Yuan, Y., Asakura, K., Wan, H., Tsai, K., and Iwasawa, Y., *Catal. Lett.* **42**, 15 (1996).
52. Wagner, F. E., Galvagno, S., Milone, C., Visco, A. M., Stievano, L., and Calogero, S., *J. Chem. Soc. Faraday Trans.* **93**, 3403 (1997).
53. Tanielyan, S. K., and Augustine, R. L., *Appl. Catal. A* **85**, 73 (1992).
54. Mathieson, T. J., Langdon, A. G., Milestone, N. B., and Nicholson, B. K., *Chem. Commun.* 371 (1998).